

## Stability of the viscous flow of a polymeric fluid past a flexible surface

Paresh Chokshi and V. Kumaran

*Department of Chemical Engineering, Indian Institute of Science, Bangalore 560 012, India*

(Received 27 June 2006; accepted 1 February 2007; published online 27 March 2007)

The instability in plane Couette flow of a viscoelastic fluid past a deformable surface is examined using the temporal linear stability theory in the zero Reynolds number limit. The polymeric fluid is described using the Oldroyd-B model and the flexible wall is modeled as a linear viscoelastic solid surface. The analysis shows that the wall flexibility tends to reduce the decay rate of the stable discrete modes for the polymeric flow past a rigid wall, and one of the discrete modes becomes unstable when the wall deformability parameter  $\Gamma = V\eta/(GR)$  exceeds a certain critical value  $\Gamma_c$ . Here,  $V$  is the top-plate velocity,  $\eta$  is the zero shear viscosity of the polymeric fluid,  $G$  is the shear modulus of the wall, and  $R$  is the width of the fluid layer. The analysis reveals the presence of two classes of modes, the first of which becomes unstable for perturbations with wavelength comparable to the channel width (finite wavelength modes), and the second becomes unstable for perturbations with wavelength small compared to the channel width (short wave modes). The latter class of modes are found to be absent for the highly concentrated polymer solutions with  $\beta \leq 0.23$ , where  $\beta$  is the ratio of solvent-to-solution viscosity. We have mapped out the regions in the parameter space ( $\bar{W}$ - $H$ ) where the finite wavelength and short wave modes are unstable, where  $\bar{W} = (\lambda G/\eta)$ , and  $\lambda$  is the relaxation time of the viscoelastic fluid. Fluid elasticity is found to have a stabilizing influence on the unstable mode, such that when the shortwave instability is absent for  $\beta \leq 0.23$ , the flow becomes stable for any Weissenberg number  $\bar{W} > \bar{W}_{\max}$ . Here,  $\bar{W}_{\max}$  increases proportional to  $H$  for  $H \gg 1$ . However, when the shortwave instability is present, the instability persists for  $\bar{W} \gg 1$ . The behavior of both classes of modes with respect to the parameters, like  $\bar{W}$ ,  $H$ ,  $\beta$ , and the ratio of solid-to-fluid viscosity  $\eta_r$ , is examined. © 2007 American Institute of Physics. [DOI: 10.1063/1.2711149]

### I. INTRODUCTION

The dynamics of fluid flow past a compliant surface is qualitatively different from that past a rigid surface because of the coupling between the fluid and wall dynamics, and the elasticity of the surface could affect the fluid flow. In particular, this coupling could influence the transition from laminar to turbulent flow in such systems. Experiments conducted by Krindel and Silberberg<sup>1</sup> indicated that the onset of laminar-to-turbulence transition in Newtonian fluid flow through gel-walled tube can occur at Reynolds number much smaller than 2100, the critical Reynolds number for the flow through a rigid tube. Motivated by this observation, extensive studies pertaining to the linear stability analysis of fluid flow in tubes and channels bounded by gel walls have been carried out. The results of these studies indicated that there are at least three modes of instability in flexible-walled tubes and channels that are qualitatively different from those in rigid tubes and channels, namely the *viscous modes*, the *wall modes*, and the *inviscid modes*, depending upon the regime of flow operation. A detailed review and classification of these instabilities have been covered by Kumaran<sup>2</sup> and Shankar.<sup>3</sup> In the present study, the attention is restricted only to the unstable viscous modes, which drive the flow past a deformable wall unstable even in the absence of inertial forces.

The linear stability analysis of Newtonian fluid flow past a flexible surface in a plane Couette setup performed by Ku-

maran *et al.*<sup>4</sup> suggested that the coupling between the fluid flow and the wall dynamics renders the flow unstable even in the limit of zero Reynolds number. The fluid-solid interface was found to become unstable when the dimensionless top plate velocity  $\Gamma = V\eta/GR$  exceeds a critical value. Here,  $V$  is the uniform velocity of the top plate,  $\eta$  is the viscosity of the fluid,  $R$  is the channel width, and  $G$  is the shear modulus of the gel wall. The instability is driven by a discontinuity in the strain rate across the fluid-gel interface, and the destabilizing mechanism is the transfer of energy from the mean flow to the fluctuations due to the shear work done by the mean flow at the interface. The experiments conducted by Kumaran and Muralikrishnan have verified the presence of an unstable mode using the parallel plate geometry of a rheometer.<sup>5,6</sup> The experimental value of critical velocity required for the onset of instability was found to be in good agreement with the theoretical predictions of Ref. 4 with no adjustable parameters, for a wide range of gel thicknesses and elastic moduli. This class of modes in inertialess motion are referred to as “viscous modes” of flow past a flexible surface and will be referred to as the KFP modes in the present paper. The analysis was extended to the viscous flow through a flexible tube by Kumaran.<sup>7</sup>

Fluids encountered in biological systems are likely to be viscoelastic, and it is essential to analyze the stability behavior of viscoelastic fluid past a compliant surface. For the flow of viscoelastic fluid past a rigid wall, significant work has been carried out to study the stability behavior and investi-

gate the nature of the eigenspectrum for the growth rate. In most prior studies, the viscoelastic fluid is described either by the *upper convected Maxwell* (UCM) model or the *Oldroyd-B* model, wherein the polymer chains are treated as the elastic dumbbells. In one of the oldest studies, Gorodtsov and Leonov<sup>8</sup> performed a linear stability analysis of UCM fluid for zero Reynolds number flow. Providing the closed form solution of the problem, they showed that there exist precisely two discrete modes accompanied by a *stable* continuous spectrum. Both the discrete modes have the same rate of decay but different values of frequency. These viscous modes (abbreviated as GL modes in the current paper) have been reported to be stable to infinitesimal perturbations with any value of axial wave number and for a fluid with a wide range of elasticity, in the absence of inertia. Renardy<sup>9</sup> further provided a rigorous proof of stability at zero Reynolds number for any arbitrary value of fluid elasticity, represented by the Weissenberg number,  $W = \lambda V/R$ , where  $\lambda$  is the relaxation time of the UCM fluid. Another simple but widely accepted model for the polymeric solutions, the Oldroyd-B model, has also been investigated for linear stability in plane Couette as well as with an additional Poiseuille component for zero Reynolds number flow.<sup>10</sup> The authors present a comprehensive picture of the eigenspectrum for the problem using the spectral method. For an Oldroyd-B fluid, which is a generalization of the UCM model for polymer solutions, the GL modes of the UCM model persist with slight modification. The original GL modes for the UCM fluid become more stable (i.e., the decay rate increases) due to the presence of solvent viscosity. These two GL modes modified by the solvent contribution in the Oldroyd-B model will still be referred to as GL modes in what follows. Apart from these two GL modes in Oldroyd-B fluid, there also exist two *stable* continuous spectra along which the coefficient of the highest derivative in the governing equation for the growth rate is zero. The first one is the same as that for the UCM fluid, whereas the second one is qualitatively different. While the solutions for the governing equations for growth rate are analytic for the continuous spectrum for the UCM fluid, it ceases to be analytic and has a branch cut along the second continuous spectrum. As a consequence, the eigenvalues emerge from or disappear through the continuous spectrum as parameters change. As a result, there exist, apart from GL modes, a string of discrete eigenvalues on both sides of this second continuous spectrum.

While the problem of viscoelastic fluid past a hard surface has received significant attention, the flow of such fluid past a deformable surface is largely uncovered. Recently, Shankar and Kumar<sup>11</sup> carried out a linear stability analysis of the UCM fluid in plane Couette flow past gel in the creeping flow limit. The analysis predicts *unstable* viscous modes even in the limit of zero Reynolds number when parameter  $\Gamma = V\eta/(GR)$  exceeds a certain critical value. Their analysis recovers the stable modes for UCM fluid flow past a rigid surface reported in Ref. 8 (the GL modes) as well as the unstable viscous mode for Newtonian fluid flow past gel of Ref. 4 (the KFP mode). Their analysis shows that the wall elasticity has a destabilizing effect on one of the two discrete GL modes, whereas finite fluid elasticity has a stabilizing

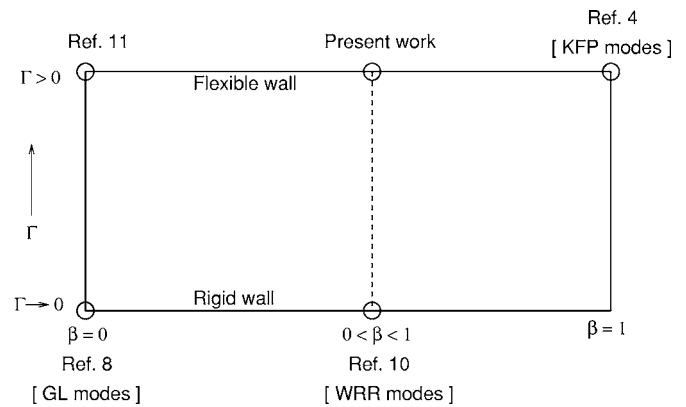


FIG. 1. Schematic illustration of the present work put into perspective with regard to the previous analyses.  $\Gamma \rightarrow 0$  indicates the rigid wall limit and nonzero  $\Gamma$  the flexible wall case. The solvent-to-solution viscosity ratio  $\beta$  is unity for the Newtonian fluid and zero for the UCM fluid.

effect on the unstable KFP mode for the Newtonian fluid. Since the UCM model ignores the viscous contribution due to the solvent, it is suitable for the polymer melt. In the present study, we consider more general Oldroyd-B fluid, which takes into account the solvent contribution, and hence represents the polymer solution. As indicated earlier, there are solutions for the growth rate for an Oldroyd-B model that do not exist for the UCM model, and it is of interest to examine the effect of a flexible wall on these modes, in order to have a comprehensive understanding of the stability of a viscous flow past a flexible surface. The scope of the present work, in relation to the previous analyses,<sup>4,10,11</sup> is illustrated schematically in Fig. 1. It was also verified that the previous results are recovered in their respective limits.

The organization of the rest of the paper is as follows. The set of governing equations, their steady-state solution, and the formulation of the temporal linear stability problem are presented in Sec. II. In Sec. III, the viscous mode instability for an Oldroyd-B fluid flow past gel is analyzed and the stability diagrams are constructed for a wide range of parameters. The conclusions of the analysis are discussed in Sec. IV.

## II. PROBLEM FORMULATION

### A. Governing equations

The coordinate system and base flow configuration are shown in Fig. 2. The system consists of an incompressible viscoelastic fluid of density  $\rho$  occupying the domain  $0 < y^*$

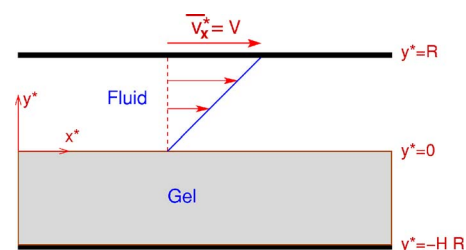


FIG. 2. Schematic diagram of plane Couette flow over a flexible surface showing the dimensional coordinate system.

$< R$ . The polymeric solution is characterized by the zero-shear viscosity  $\eta$  and the relaxation time  $\lambda$ . The fluid is supported on an incompressible linear viscoelastic gel medium of density the same as that for the fluid  $\rho$  and thickness  $HR$ . The rigid wall at  $y^* = R$  is set moving in the  $x$  direction with velocity  $\bar{v}_x^* = V$  whereas the bottom rigid wall at  $y^* = -HR$ , which supports the gel, is held stationary. Here and in what follows, the quantities with a superscript  $*$  are dimensional and the ones without the superscript are dimensionless unless stated otherwise. The fluid mass and momentum balance equations in the zero Reynolds number limit are

$$\nabla \cdot \mathbf{v} = 0, \quad (1)$$

$$-\nabla p_f + \nabla \cdot \boldsymbol{\tau} = 0, \quad (2)$$

where  $\mathbf{v}$  denotes the fluid velocity field and  $p_f$  is the fluid pressure. For the Oldroyd-B model, the stress tensor  $\boldsymbol{\tau}$  consists of the viscous stress due to the solvent ( $\boldsymbol{\tau}^s$ ) and the polymeric stress ( $\boldsymbol{\tau}^p$ ),

$$\boldsymbol{\tau} = \boldsymbol{\tau}^s + \boldsymbol{\tau}^p. \quad (3)$$

The viscous stress arising due to the solvent viscosity ( $\eta_s$ ) is given by Newton's law of viscosity,

$$\boldsymbol{\tau}^s = \beta[\nabla \mathbf{v} + (\nabla \mathbf{v})^T], \quad (4)$$

where the superscript  $T$  indicates the transpose, and the parameter  $\beta = \eta_s / \eta$ , known as the retardation parameter, is introduced to represent the solvent contribution to the solution viscosity  $\eta$ , where  $\eta = \eta_s + \eta_p$ . The polymer contribution is given by  $(1 - \beta) = \eta_p / \eta$ .

The polymeric stress  $\boldsymbol{\tau}^p$  is expressed in terms of the polymer chain conformation tensor  $\mathbf{c}$ , which is given by the single relaxation time constitutive model,

$$\mathcal{D}_t \mathbf{c}^* = -\frac{(\mathbf{c}^* - \mathbf{c}^{*eq})}{\lambda}. \quad (5)$$

The material time derivative  $\mathcal{D}_t \mathbf{c}^*$  is the upper convected time derivative of  $\mathbf{c}$  defined as

$$\mathcal{D}_t \mathbf{c}^* = \partial_t \mathbf{c}^* + \mathbf{v}^* \cdot \nabla \mathbf{c}^* - \mathbf{c}^* \cdot (\nabla \mathbf{v}^*) - (\nabla \mathbf{v}^*)^T \cdot \mathbf{c}^*. \quad (6)$$

Under no-flow conditions, the equilibrium chain conformation is  $\mathbf{c}^{*eq} = (k_B T / H) \delta_{ij}$ , where  $H$  is the spring constant and  $k_B T$  is the thermal energy. The polymeric stress, which is proportional to the departure of the conformation tensor from its equilibrium value, is given by the expression

$$\boldsymbol{\tau}^{*p} = \frac{\eta_p H}{\lambda k_B T} (\mathbf{c}^* - \mathbf{c}^{*eq}). \quad (7)$$

Upon nondimensionalizing  $\mathbf{c}$  with  $(k_B T / H)$ ,  $\boldsymbol{\tau}^p$  with  $\eta V / R$  and time with  $R / V$ , the constitutive model equations become

$$\mathcal{D}_t \mathbf{c} = -\frac{(\mathbf{c} - \mathbf{I})}{W}, \quad (8)$$

$$\boldsymbol{\tau}^p = (1 - \beta) \frac{(\mathbf{c} - \mathbf{I})}{W}, \quad (9)$$

where Weissenberg number  $W = (\lambda V / R)$  is the dimensionless relaxation time of the Oldroyd-B fluid, and  $\mathbf{I}$  is an identity tensor.

Substituting the expressions of  $\boldsymbol{\tau}^s$  and  $\boldsymbol{\tau}^p$  in the momentum conservation equation (2), we obtain

$$0 = -\nabla p_f + \beta \nabla^2 \mathbf{v} + \nabla \cdot \boldsymbol{\tau}^p. \quad (10)$$

The momentum conservation equation for the Newtonian fluid is recovered in the limit  $W \rightarrow 0$  as well as for  $\beta = 1$ , and the governing equation for the upper convected Maxwell (UCM) fluid is obtained for  $\beta = 0$ .

The flexible wall is modeled as an incompressible linear viscoelastic solid. A similar model has been previously used to analyze the stability of the flow past a deformable wall.<sup>4,7,11,12</sup> The dynamics of solid wall is described by a displacement field  $\mathbf{u}$  given by

$$\nabla \cdot \mathbf{u} = 0, \quad (11)$$

$$0 = -\nabla p_g + \nabla \cdot \boldsymbol{\sigma}. \quad (12)$$

Here, the pressure  $p_g$  and the stress tensor  $\boldsymbol{\sigma}$  for the gel are scaled with  $\eta V / R$ , the viscous stress in the fluid. The stresses in the solid are comprised of the elastic and the viscous contributions,

$$\boldsymbol{\sigma}^* = G[\nabla \mathbf{u}^* + (\nabla \mathbf{u}^*)^T] + \eta_g \partial_t^* [\nabla \mathbf{u}^* + (\nabla \mathbf{u}^*)^T], \quad (13)$$

where  $G$  is the shear modulus and  $\eta_g$  is the viscosity of the gel medium. The solid stress tensor in dimensionless form is given by

$$\boldsymbol{\sigma} = \left( \frac{1}{\Gamma} + \eta_r \partial_t \right) [\nabla \mathbf{u} + (\nabla \mathbf{u})^T], \quad (14)$$

where  $\Gamma = V \eta / (GR)$ , and  $\eta_r = \eta_g / \eta$  is the ratio of gel-to-fluid viscosity. Physically,  $\Gamma$  is the ratio of the viscous stresses in fluid to the elastic stresses in the gel wall. The rigid wall is recovered in the limit  $G \rightarrow \infty$ , that is,  $\Gamma \rightarrow 0$ .

The fluid-solid problem is supplemented with no-slip for the fluid velocity and zero solid displacement conditions at the top and bottom plates, respectively,

$$\mathbf{v} = (1, 0, 0) \quad \text{at } y = 1, \quad (15)$$

$$\mathbf{u} = (0, 0, 0) \quad \text{at } y = -H. \quad (16)$$

The continuity of velocities and stresses is imposed at the fluid-solid interface,

$$\mathbf{v} = \partial_t \mathbf{u}, \quad (17)$$

$$-p_f \mathbf{n} + \boldsymbol{\tau} \cdot \mathbf{n} = -p_g \mathbf{n} + \boldsymbol{\sigma} \cdot \mathbf{n} + T \mathbf{n} (\nabla_s \cdot \mathbf{n}), \quad (18)$$

where  $\mathbf{n}$  is the unit normal to the interface.  $T$  is the dimensionless interfacial tension defined as  $T = \gamma / (\eta V)$ , where  $\gamma$  is the dimensional interfacial tension between the fluid and the solid.

Finally, we would like to make a comment on the scalings used to nondimensionalize the quantities. While  $\eta / G$  seems to be an appropriate time scale for a viscous flow, we

scaled time with  $R/V$ , as done previously by Shankar and Kumar.<sup>11</sup> In the stability analysis for the present problem, we arrive at the unstable modes by continuing the already reported modes for the rigid wall to the wall with nonzero deformability, as will be seen in Sec. III C. The present scaling allows us to perform this exercise for a finite Weissenberg number. In case the time had been scaled with  $\eta/G$ , the Weissenberg number ( $\lambda G/\eta$ ) would diverge in the rigid wall limit  $G \rightarrow \infty$ . For the rigid wall problem, the time has been scaled with  $R/V$  for the creeping flow.<sup>8,10</sup>

## B. Base state

For the steady-state base flow shown in Fig. 2, the fluid velocity, the gel displacement, and the stresses are given as

$$\bar{\mathbf{v}} = (y, 0, 0),$$

$$\bar{u}_x = \Gamma(y + H), \quad \bar{u}_y = 0, \quad \bar{u}_z = 0,$$

$$\bar{\mathbf{c}} = \begin{pmatrix} 1 + 2W^2 & W & 0 \\ W & 1 & 0 \\ 0 & 0 & 1 \end{pmatrix}, \quad \bar{\boldsymbol{\tau}}^p = (1 - \beta) \begin{pmatrix} 2W & 1 & 0 \\ 1 & 0 & 0 \\ 0 & 0 & 0 \end{pmatrix}, \quad (19)$$

$$\bar{\tau}_{xy} = 1, \quad \bar{\tau}_{xx} - \bar{\tau}_{yy} = 2(1 - \beta)W, \quad (20)$$

$$\bar{\sigma}_{xy} = 1, \quad \bar{\sigma}_{xx} = 0, \quad \bar{\sigma}_{yy} = 0, \quad (21)$$

$$\bar{p}_f = \bar{p}_g = \text{const.}$$

The above base state solution satisfies the normal and tangential velocity and stress continuity conditions at the interface, which, for the base state, is flat at  $y=0$ . As the polymeric fluid exerts the normal stresses, the first normal stress difference for the viscoelastic fluid is nonzero,  $\bar{\tau}_{xx} - \bar{\tau}_{yy} = 2(1 - \beta)W$ . This additional stress, which is absent for the Newtonian fluid ( $\beta=1$  or  $W=0$ ), can play a significant role in the stability of the base flow, especially in the limit  $W \gg 1$ .

## C. Linear stability analysis

The above base flow is superimposed with two-dimensional infinitesimal amplitude disturbance of the form

$$\phi' = \tilde{\phi}(y)e^{ik(x-ct)}, \quad (22)$$

where  $k$  is the streamwise wave number,  $c$  is the complex wave speed, and  $\phi$  is a general perturbation quantity  $\phi = [\mathbf{v}, p_f, \mathbf{c}, \mathbf{u}, p_g]$ . Note that the scalar wave speed  $c$  is different from the conformation tensor  $\mathbf{c}$ .

Substituting  $\phi = \bar{\phi} + \phi'$  in the fluid and gel governing equations, we get, after linearizing, the following equations for the fluid perturbation quantities:

$$d_y \tilde{v}_y + ik \tilde{v}_x = 0, \quad (23)$$

$$-ik \tilde{p}_f + \beta(d_y^2 - k^2) \tilde{v}_x + \frac{(1 - \beta)}{W} (d_y \tilde{c}_{xy} + ik \tilde{c}_{xx}) = 0, \quad (24)$$

$$-d_y \tilde{p}_f + \beta(d_y^2 - k^2) \tilde{v}_y + \frac{(1 - \beta)}{W} (d_y \tilde{c}_{yy} + ik \tilde{c}_{xy}) = 0, \quad (25)$$

$$ik(y - c) \tilde{c}_{xx} - 2ik \tilde{c}_{xx} \tilde{v}_x - 2\tilde{c}_{xy} d_y \tilde{v}_x - 2\tilde{c}_{xy} = -\frac{1}{W} \tilde{c}_{xx}, \quad (26)$$

$$ik(y - c) \tilde{c}_{xy} - ik \tilde{c}_{xx} \tilde{v}_y - \tilde{c}_{yy} d_y \tilde{v}_x - \tilde{c}_{yy} = -\frac{1}{W} \tilde{c}_{xy}, \quad (27)$$

$$ik(y - c) \tilde{c}_{yy} - 2ik \tilde{c}_{xy} \tilde{v}_y - 2\tilde{c}_{yy} d_y \tilde{v}_y = -\frac{1}{W} \tilde{c}_{yy}. \quad (28)$$

Substituting the expressions for the components of the conformation tensor in the momentum conservation equations (24) and (25) and eliminating the pressure, we obtain a single fourth-order differential equation of the form

$$(1 - \beta)[(S^2 D^2 - 2ikWSD - 2k^2 W^2 - k^2 S^2)(D^2 + 2ikWD - 2k^2 W^2 - k^2) \tilde{v}_y] + \beta S^3 (D^2 - k^2)^2 \tilde{v}_y = 0, \quad (29)$$

or in alternative form

$$(1 - \beta)(D^2 - k^2) \left[ \frac{1}{S} (D^2 + 2ikWD - 2k^2 W^2 - k^2) \tilde{v}_y \right] + \beta (D^2 - k^2)^2 \tilde{v}_y = 0, \quad (30)$$

where  $S = 1 + ikW(y - c)$  and  $D = d/dy$ . Equation (29) is the final governing equation for the perturbations in the Oldroyd-B fluid. The governing equation for the Newtonian fluid can be recovered by setting either  $W=0$  or  $\beta=1$ , and the problem for the upper convected Maxwell (UCM) fluid is recovered for  $\beta=0$ .

The disturbance equations for the gel displacement are

$$d_y \tilde{u}_y + ik \tilde{u}_x = 0, \quad (31)$$

$$-ik \tilde{p}_g + \left( \frac{1}{\Gamma} - ikc \eta_r \right) (d_y^2 - k^2) \tilde{u}_x = 0, \quad (32)$$

$$-d_y \tilde{p}_g + \left( \frac{1}{\Gamma} - ikc \eta_r \right) (d_y^2 - k^2) \tilde{u}_y = 0. \quad (33)$$

Upon eliminating  $\tilde{p}_g$ , we obtain the following fourth-order differential equation for the normal displacement,

$$\left( \frac{1}{\Gamma} - ikc \eta_r \right) (d_y^2 - k^2)^2 \tilde{u}_y = 0. \quad (34)$$

The boundary conditions at the top and bottom plates are

$$\tilde{v}_y(1) = \tilde{v}_x(1) = 0, \quad (35)$$

$$\tilde{u}_y(-H) = \tilde{u}_x(-H) = 0.$$

The normal and tangential velocity and stress continuity conditions are applied at the perturbed interface with linearized unit normal  $\mathbf{n} = (-\partial u'_y / \partial x, 1, 0)$ . These conditions upon expanding about the flat interface and linearizing the resulting equations in the perturbation variables give the following conditions to be imposed at  $y=0$ :

$$v'_y = \partial u'_y \rightarrow \tilde{v}_y = -ikc \tilde{u}_y, \quad (36)$$

$$v'_x + \frac{d\bar{v}_x}{dy} u'_y = \partial_t u'_x \rightarrow \bar{v}_x + \bar{u}_y = -ikc\bar{u}_x, \quad (37)$$

$$\begin{aligned} \tau'_{xy} - (\bar{\tau}_{xx} - \bar{\tau}_{yy}) \left( \frac{\partial u'_y}{\partial x} \right) &= \sigma'_{xy} \rightarrow \bar{\tau}_{xy} - 2ikW(1-\beta)\bar{u}_y \\ &= \bar{\sigma}_{xy}, \end{aligned} \quad (38)$$

$$\begin{aligned} -p'_f + \tau'_{yy} &= -p'_g + \sigma'_{yy} - T \left( \frac{\partial^2 u'_y}{\partial x^2} \right) \rightarrow -\bar{p}_f + \bar{\tau}_{yy} = -\bar{p}_g \\ &+ \bar{\sigma}_{yy} + Tk^2\bar{u}_y. \end{aligned} \quad (39)$$

Here, the stresses are given by the respective constitutive models. The second terms on the left side of the tangential velocity [Eq. (37)] and the tangential stress continuity [Eq. (38)] conditions express the coupling between the mean flow and the perturbation quantities. These two terms arise due to the discontinuity across the fluid-gel interface in the shear rate and the first normal stress difference in the base state, respectively. The term containing  $T$  in the condition (39) represents the surface force due to the scaled interfacial tension  $T=(\gamma/\eta V)$ , where  $\gamma$  is the dimensional surface tension.

### III. ANALYSIS

In this section, we analyze the viscous mode instability arising purely by the interplay of the viscous and the elastic forces in the Oldroyd-B fluid and the elastic force in the solid. The final governing equations for the fluid [Eq. (29)] and the solid [Eq. (34)] are solved numerically, the boundary conditions (35) and the interface conditions (36)–(39) are imposed, and the complex wave speed  $c$  is obtained as the eigenvalue of the stability problem. Perturbations are unstable for  $c_i > 0$ , and stable for  $c_i < 0$ .

#### A. Background

For an upper convected Maxwell (UCM) fluid flow past a rigid wall, Gorodtsov and Leonov reported two discrete modes, referred to as GL modes in the present paper, as well as a continuous spectrum.<sup>8</sup> Both discrete modes have the same growth rate, and were found to be stable for any value of the Weissenberg number. The continuous spectrum is a consequence of singularity in the final governing equation (29), which results when the coefficient of the largest derivative vanishes. For the UCM fluid ( $\beta=0$ ), the condition for singularity is  $S=0$ , which gives the continuous spectrum with the imaginary part of wave speed  $c_i=-1/(kW)$  and real part  $c_r=y$ , that is,  $0 \leq c_r \leq 1$ . Since  $c_i$  is negative, the continuous spectrum is always stable.

For an Oldroyd-B fluid ( $0 < \beta < 1$ ) flow past a hard wall, the two discrete GL modes are modified by the solvent contribution to the viscosity, but they remain stable.<sup>10</sup> Apart from these two discrete modes, there exist two continuous spectra, which are a consequence of the singularity in Eq. (29). The singularity condition for the UCM fluid holds for the Oldroyd-B fluid, hence the continuous spectrum for the UCM fluid exists for the Oldroyd-B fluid as well. The other continuous spectrum for the Oldroyd-B fluid results from the

singularity condition,  $(1-\beta)S^2 + \beta S^3 = 0$ . This gives a stable continuous spectrum with  $c_i=-1/(k\beta W)$  and real part  $c_r=y$ . This continuous spectrum is due to a branch cut, and is accompanied by a string of discrete eigenvalues on either side of it, whose number depends upon the value of  $\beta$ .<sup>10</sup>

For UCM fluid, Shankar and Kumar<sup>11</sup> continued the two discrete GL modes for a rigid channel to a nonzero finite value of wall deformability using a linear viscoelastic model for the deformable solid wall. While one of the GL modes remains stable, the other one was found to become unstable when the wall deformability parameter,  $\Gamma=V\eta/(GR)$ , exceeds a certain finite value  $\Gamma_t$  for transition. This demonstrated the destabilizing effect of wall flexibility on one of the GL modes. This unstable GL mode was shown to be the continuation of an unstable mode for the Newtonian fluid flow past gel, the KFP mode,<sup>4</sup> to the fluid with nonzero elasticity. The present study is an extension of the investigations carried out by Refs. 4, 10, and 11, as illustrated schematically in Fig. 1.

#### B. Numerical method

For plane Couette flow of a UCM fluid, the governing equations for the fluid as well as the solid gel exhibit the exact solutions. Upon imposing the boundary and the interface conditions on the solution, one obtains a characteristic equation that is sixth-order polynomial in wave speed  $c$ .<sup>11</sup> Two of these six modes are GL modes modified by the finite wall deformability. For an Oldroyd-B fluid, however, the fluid governing equation results in solutions that are hypergeometric functions.<sup>10</sup> The characteristic equation is, therefore, a transcendental equation in  $c$ , which needs to be solved numerically. In the present analysis, instead of using the exact solution in the form of hypergeometric functions, we numerically integrate the governing equations using the *shooting technique* on the adaptive grid and solve the characteristic equation, obtained by imposing the interface conditions, for  $c$  using the Newton-Raphson method. The numerical scheme is discussed in detail in Ref. 13, and has been used previously to study the stability of the Newtonian fluid<sup>13,14</sup> as well as the viscoelastic fluid<sup>12</sup> flow past a flexible surface. Apart from the shooting method, we also use the spectral method to construct the entire eigenspectrum of the problem. In this method, the linear differential operator of the generalized eigenvalue problem is discretized using the Chebyshev-tau technique and the eigenspectrum is obtained using the QZ algorithm (available with the IMSL package). We use the spectral method mainly to verify the results obtained from the shooting method. Irrespective of the numerical technique employed, we obtain the dispersion relation of the form

$$\mathcal{F}(c, k, \Gamma, W, \beta, H, \eta_r) = 0. \quad (40)$$

The root of this equation is wave speed  $c$ . For neutral stability, the dimensionless transition velocity  $\Gamma_t = \mathcal{G}(k, W, \beta, H, \eta_r)$  is obtained by setting  $c_i=0$ .

The numerical method has been verified by recovering the previously reported results. The viscous modes for a flow past a rigid wall are captured in the limit  $G \rightarrow \infty$ . Figure 3

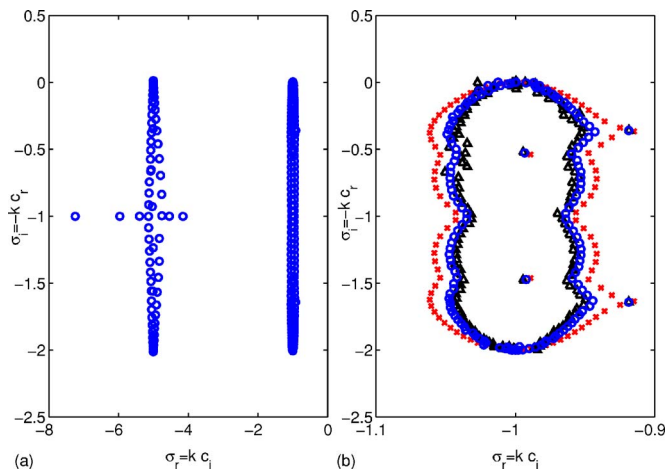


FIG. 3. Eigenspectrum of the growth rate for plane Couette flow of an Oldroyd-B fluid past a rigid wall with base flow  $\bar{v}_x=2y$ , where  $0 \leq y \leq 1$  for  $k=1$ ,  $W=1$ ,  $\beta=0.2$ . (a) Entire spectrum for 70 Chebyshev modes; (b) enlarged view near the first continuous spectrum for different number of Chebyshev modes ( $n$ );  $\times$ ,  $n=50$ ;  $\circ$ ,  $n=70$ ;  $\triangle$ ,  $n=80$ .

shows the eigenspectrum of the growth rate  $\sigma=-ikc$  for an Oldroyd-B fluid flow past a rigid wall. This spectrum, obtained by the spectral method using 70 Chebyshev modes, is qualitatively similar to Fig. 3 of Ref. 10. In order to reproduce the spectrum, we considered the same base state as used by them, that is, dimensionless axial velocity being  $\bar{v}_x=2y$ . In this spectrum, the two least stable modes, with the largest growth rate  $\sigma_r$ , are the discrete GL modes modified by the nonzero solvent viscosity ( $\beta=0.2$ ). Apart from the GL modes, we also notice two poorly resolved continuous spectra and a string of discrete modes associated with the second continuous spectrum. The eigenspectrum in the vicinity of the first continuous spectrum is enlarged in Fig. 3(b) for three different refinements of the Chebyshev discretizations. Two discrete GL modes are clearly shown to be well converged for the number of Chebyshev polynomials  $n=70$  and 80. However, the continuous spectrum, which theoretically should be a line segment at  $\sigma_r=-1$ , appears as a balloon with its width narrowing upon increasing the number of Chebyshev modes, indicating poor convergence for the eigenvalues corresponding to the singular solutions.<sup>10</sup> It is important to note that all the subsequent results, except Fig. 4, are obtained using the shooting method such that the eigenvalues and the transition parameter  $\Gamma_t$  are well converged to nine decimal places. The Chebyshev-tau method is used only to generate Fig. 4 in order to show the influence of wall flexibility on the entire eigenspectrum.

### C. Effect of wall flexibility

The evolution of the eigenspectrum upon increasing the wall deformability parameter  $\Gamma$  (which is equivalent to reducing the shear modulus of the solid gel from  $G \rightarrow \infty$  to a finite value) is shown in Fig. 4 for the base flow  $\bar{v}_x=2y$ . We observe that the following:

- (i) The two discrete GL modes are modified significantly, such that one of them becomes unstable when  $\Gamma$  exceeds a certain transition value  $\Gamma_t$ .

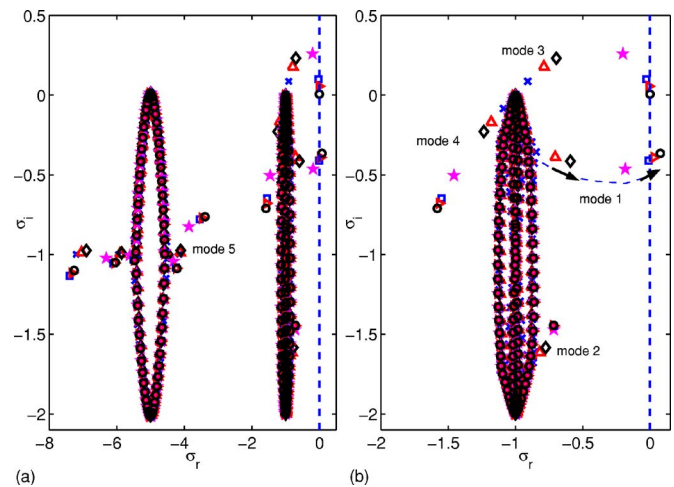


FIG. 4. Eigenspectrum of growth rate for plane Couette flow of an Oldroyd-B fluid past a flexible wall with base flow  $\bar{v}_x=2y$ , where  $0 \leq y \leq 1$  for  $k=1$ ,  $W=1$ ,  $\beta=0.2$ ,  $H=10$ ,  $\eta_r=0$ , and increasing value of wall deformability parameter  $\Gamma$ .  $\times$ ,  $\Gamma=0.01$ ;  $\triangle$ ,  $\Gamma=0.05$ ;  $\diamond$ ,  $\Gamma=0.1$ ;  $\star$ ,  $\Gamma=1.0$ ;  $\square$ ,  $\Gamma=5.0$ ;  $\triangleright$ ,  $\Gamma=10.0$ ;  $\circ$ ,  $\Gamma=100.0$ . (a) Entire spectrum; (b) enlarged view near the first continuous spectrum. The arrows show the trail of mode 1 as  $\Gamma$  is increased.

- (ii) A few additional discrete modes emerge from both the continuous spectra.
- (iii) Both the continuous spectra present in the rigid wall case remain unchanged, because the singularity of the fluid governing equation remains unchanged by the presence of a flexible wall.

In Fig. 4, modes 1 and 2 are the two discrete GL modes for different values of  $\Gamma$ . Of these, mode 1 becomes unstable when  $\Gamma$  exceeds the value of 5. Modes 3, 4, and 5 denote the additional discrete modes that emerge from the continuous spectra upon increasing  $\Gamma$ . The variation of the growth rates for the first five least stable discrete modes with wall deformability is shown in Fig. 5. The real part of the growth rate for mode 1 becomes positive for  $\Gamma \geq 5.0$ , whereas that for the second GL mode remains negative [see Fig. 5(a)]. The three additional modes also remain stable for any large value of wall deformability  $\Gamma$ . These three modes merge with the continuous spectra as  $\Gamma$  approaches zero (rigid wall limit). The least stable of these three modes, mode 3, becomes neutrally stable for  $\Gamma \gg 1$ . The scalings of the growth rate for the first four discrete modes with  $\Gamma$  are shown in Fig. 5(d).

For the base flow of interest,  $\bar{v}=y$ , Fig. 6 shows the effect of  $\Gamma$  on the GL modes for different values of  $\beta$  and for fixed  $k$ ,  $W$ ,  $H$ , and  $\eta_r$ . The curve for the UCM fluid ( $\beta=0$ ) is in agreement with the result of Ref. 11. The imaginary part of wave speed  $c_i$  remains negative for one mode, whereas  $c_i$  becomes positive for  $\Gamma > \Gamma_t$  rendering the other mode unstable. When time is scaled with the flow-independent quantity  $\eta/G$ ,  $\Gamma [=V\eta/(GR)]$  becomes the dimensionless top plate velocity and  $\Gamma_t$  is the dimensionless top plate velocity for the onset of instability.<sup>4</sup> The variation of  $\Gamma_t$  with  $\beta$  is shown in Fig. 7 for different values of the Weissenberg number. For  $\beta=0$ , we get the results for UCM fluid, whereas for  $\beta=1$ , we recover the KFP mode of Newtonian fluid reported in Ref. 4. Contrary to the behavior for the rigid wall case where the

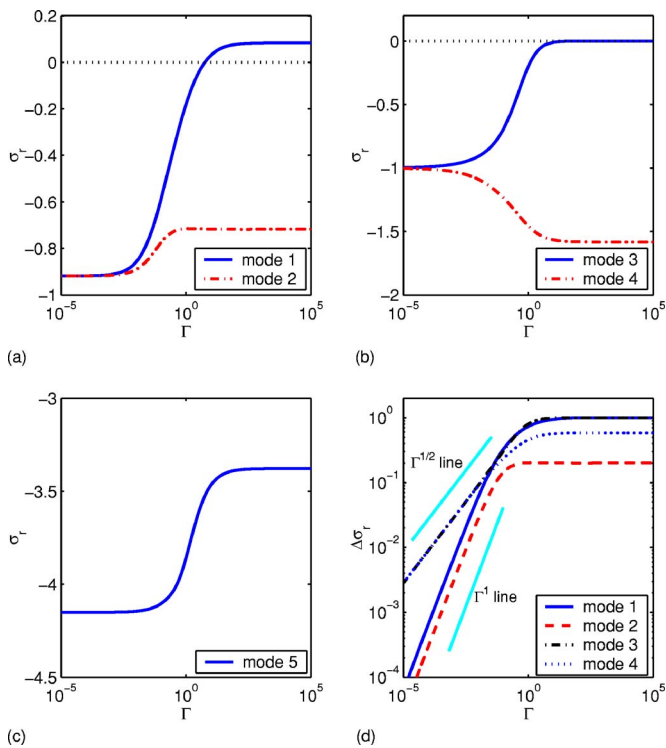


FIG. 5. Variation of growth rate of the first few discrete modes with wall flexibility parameter  $\Gamma$  for the same values of parameters as in Fig. 4. (a) The GL modes: mode 1 and mode 2; (b) the discrete mode 3 and mode 4; (c) the discrete mode 5; (d) variation of  $\Delta\sigma_r$  with  $\Gamma$ . Here  $\Delta\sigma_r = \sigma_r - \sigma_r|_{\Gamma=0}$ .

increasing solvent contribution (increasing  $\beta$ ) further stabilizes the GL modes,<sup>10</sup> the influence of increasing solvent viscosity is found to be destabilizing for the flexible wall case. This is due to the mechanism of viscous instability for the flexible wall case wherein the increasing fluid viscosity has a destabilizing effect in the absence of fluid inertia.

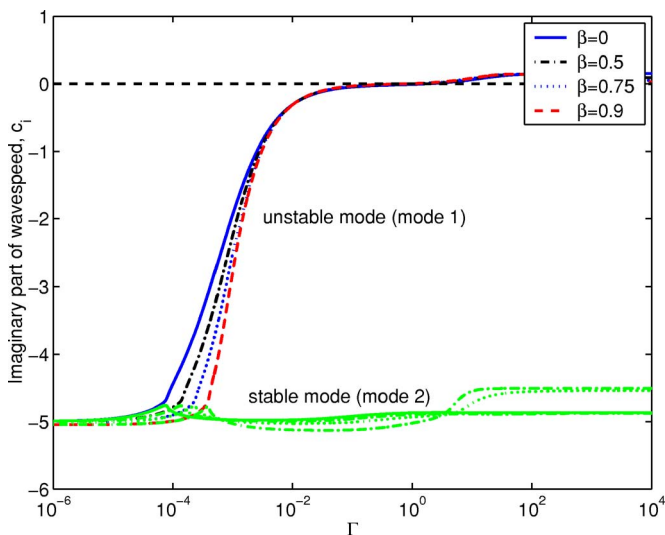


FIG. 6. Effect of wall deformability on GL modes: Imaginary part of the wave speed as a function of  $\Gamma$  for  $k=0.01$ ,  $H=20$ ,  $W=20$ ,  $\eta_r=0$ , and different values of  $\beta$ .

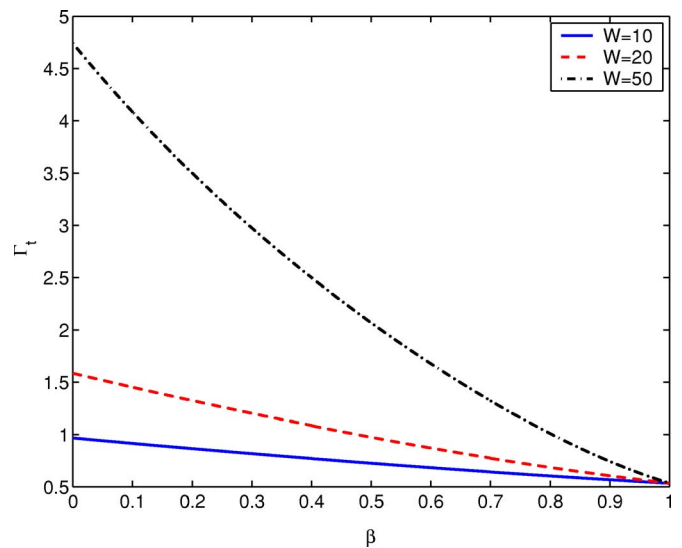


FIG. 7. Transition parameter  $\Gamma_t$  as a function of  $\beta$  for  $k=0.01$ ,  $H=20$ ,  $\eta_r=0$ , and different values of  $W$ .

**D. Effect of fluid elasticity**

The stabilizing influence of fluid elasticity can be further established by analyzing the effect of fluid Weissenberg number on the growth rate. For this, we start with the unstable KFP mode for the Newtonian fluid flow past a flexible wall for fixed  $\Gamma$  and study the effect of increasing fluid elasticity on it. Figure 8 shows  $c_i$  of the unstable KFP mode as a function of the Weissenberg number for two different values of  $\Gamma$ . For  $\Gamma=2.0$ , on introducing the elastic effect in otherwise viscous fluid,  $c_i$  decreases and becomes negative at  $W \approx 10-100$ , as shown in Fig. 8(a). Thus, the unstable KFP mode is stabilized upon introducing the fluid elasticity. In the limit of  $W \rightarrow \infty$ ,  $c_i$  approaches zero from the negative side following the scaling law  $c_i \sim -1/W$ , which incidentally is the scaling law for both the continuous spectra, whereas for  $\Gamma=20$ ,  $c_i$  decreases with increasing  $W$  but remains positive

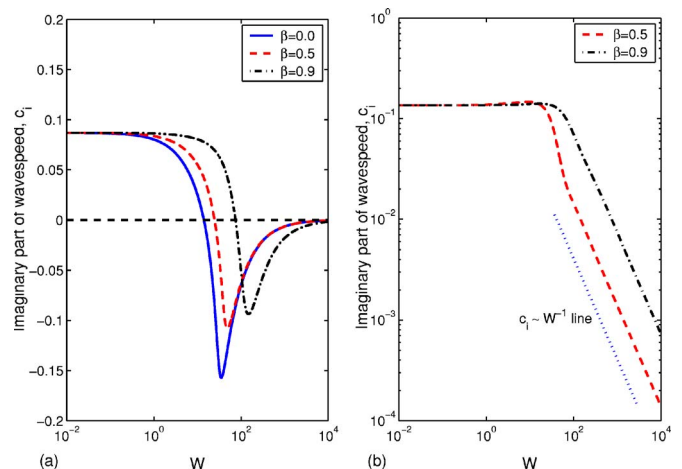


FIG. 8. Effect of fluid elasticity on KFP mode: Imaginary part of wave speed as a function of  $W$  for  $H=20$ ,  $k=0.05$ , and  $\eta_r=0$ . (a)  $\Gamma=2.0$ ; (b)  $\Gamma=20$ .

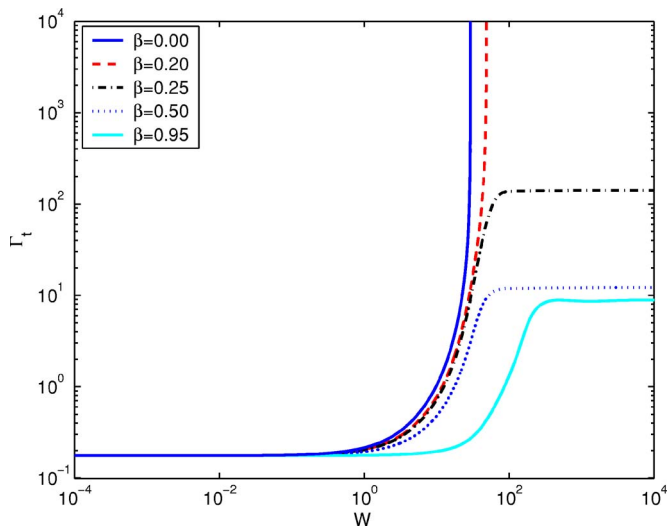


FIG. 9. Transition parameter  $\Gamma_t$  against Weissenberg number for  $k=0.05$ ,  $H=20$ , and  $\eta_r=0$ .

for any large value of  $W$  and approaches zero from the positive side as  $W \rightarrow \infty$ , following the scaling law  $c_i \sim 1/W$ , as shown in Fig. 8(b).

### E. Neutral stability diagrams

All the above discussed results are condensed in Fig. 9 in the form of a neutral stability diagram in the  $W$ - $\Gamma_t$  plane for a fixed wave number. Here, the transition parameter  $\Gamma_t$  is shown to increase with Weissenberg number. The figure suggests two distinctive zones of  $\beta$  in which the stability behavior for a large Weissenberg number is qualitatively different. For  $0 \leq \beta \leq 0.23$ , there exists a Weissenberg number beyond which the unstable mode ceases to exist, thus rendering stability to the system. The behavior in this range of  $\beta$  is qualitatively similar to the findings for the UCM fluid ( $\beta=0$ ).<sup>11</sup> On the contrary, for  $0.23 \leq \beta < 1$ , there exists a flat region such that  $\Gamma_t$  is independent of Weissenberg number for  $W \gg 1$ . Hence, the unstable mode persists for any large value of the Weissenberg number.

The critical wall deformability parameter  $\Gamma_c$  is obtained as the point of minimum  $\Gamma_t$  on the  $k$ - $\Gamma_t$  curve. Figure 10(a) shows the typical neutral stability diagrams for  $W=10$  and  $H=10$  and different values of  $\beta$ . For  $\beta=0$ , the curve has a distinctive point of minimum  $\Gamma_t$  at a finite wave number  $k_c \sim O(1)$ , with  $\Gamma_t$  diverging as  $1/k$  for  $k \ll 1$  and diverging faster than  $k$  for  $k \gg 1$ . Though not shown, this behavior is observed for  $\beta$  close to zero ( $\beta \leq 0.23$ ) and is qualitatively similar to that for the Newtonian fluid ( $\beta=1$ ). However, in the range  $0.23 \leq \beta < 1$ , the curve has a peculiar shape such that  $\Gamma_t$  attains a plateau for  $k \gg 1$ , indicating the instability for large wave-number perturbations. This shortwave instability is due to a jump in the first normal stress difference across the fluid-solid interface. While the normal stress differences are zero in the linear elastic solid, the viscoelastic fluid has a nonzero value of the first normal stress difference in the base state,  $\bar{\tau}_{xx} - \bar{\tau}_{yy} = 2(1-\beta)W$  (refer to Sec. II B). Such a jump is known to drive a shortwave instability at the interface between two flowing viscoelastic fluid layers in the

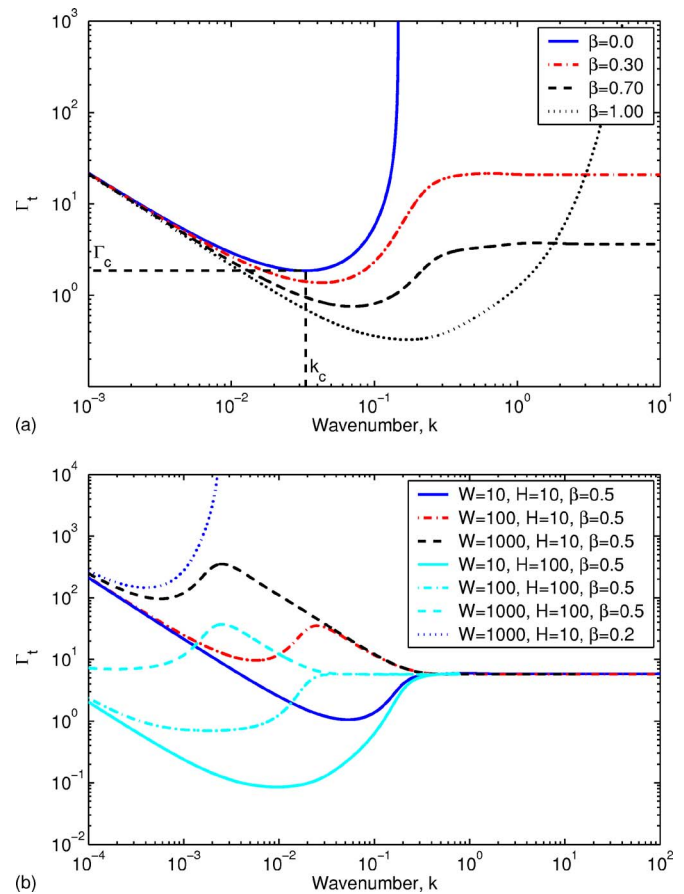


FIG. 10. Neutral stability curve  $\Gamma_t$  versus  $k$ . The point of minimum  $\Gamma_t$  on this curve corresponds to the critical point  $(k_c, \Gamma_c)$ . (a) The parameters are  $W=10$ ,  $H=10$ , and  $\eta_r=0$ ; (b) shown for different values of  $W$  and  $H$ . For  $W \gg 1$ , the critical point lies in the flat region independent of  $W$  and  $H$ .

absence of interfacial tension and inertia.<sup>15</sup> Thus, the dilute polymeric solutions with  $0.23 \leq \beta < 1$  admit the finite wave-number mode as well as the shortwave mode of instability. Interestingly, for highly elastic fluid, the shortwave mode turns out to be the critical mode since the critical parameter  $\Gamma_c$  lies on the plateau in the high wave-number region for  $W \gg 1$  as shown in Fig. 10(b). It should be noted that even though the first normal stress difference is largest for  $\beta=0$ , the shortwave instability is not observed for the UCM fluid ( $\beta=0$ ). This is apparently because the polymeric stresses are dominant over the viscous stresses in the fluid and the elastic stresses in the solid for  $\beta$  close to zero, and tend to stabilize the shortwave mode of instability.

Figure 10(b) shows that the plateau in  $\Gamma_t$  for large wave number is independent of the solid thickness  $H$ . As the stability behavior of modes with  $k \gg 1$  is unaffected by the boundary conditions at the walls away from the interface, these modes are the shortwave instability modes. This instability due to the large wave-number disturbances is believed to be similar to the shortwave instability present at the interface of two viscoelastic fluids flowing under shear, studied by Renardy in Ref. 15. The similarity is established by comparing the scalings of various quantities with those mentioned in Ref. 15 for the shortwave asymptotic. From the eigenfunctions corresponding to the high wave-number solu-

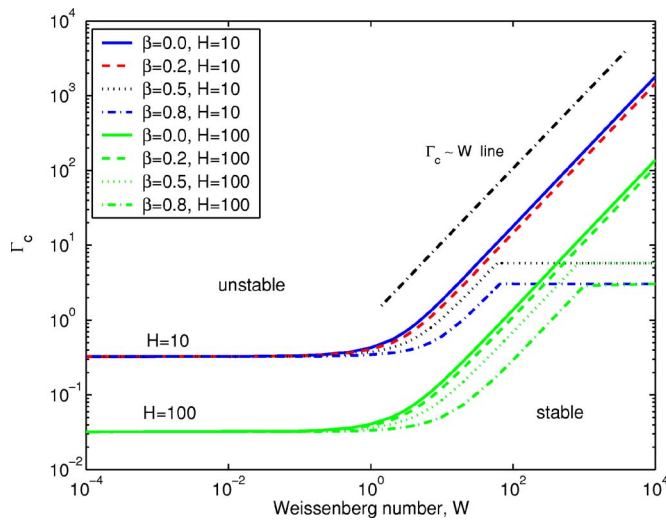


FIG. 11. Variation of the critical parameter  $\Gamma_c$  with Weissenberg number for  $\eta_r=0$ ,  $T=0$ , and different values of  $\beta$  and  $H$ . The plateau for  $W \gg 1$  is independent of  $H$ .

tions, the length scale of the disturbance can be obtained by the ratio  $|\bar{v}_y|/|d_y \bar{v}_y|$ , which is found to scale as  $1/k$  for  $k \gg 1$ . Using the normalization condition  $\bar{v}_y \sim O(1)$ , the order of magnitude of the axial perturbation velocity  $\bar{v}_x$  is found to be  $O(1)$ , and all the stress components in the fluid as well as the solid are found to scale as  $\bar{\tau}_{ij} \sim k$  and  $\bar{\sigma}_{ij} \sim k$ , respectively, for  $k \gg 1$ . The wave speed of the shortwave mode scales as  $c_r \sim 1/k$  for  $k \gg 1$ , thus supporting the fact that the shortwave mode travels with the interface velocity in the base state, which is zero in the present problem. Also, the leading-order growth rate,  $\sigma = -ikc$ , is  $O(1)$  for the large wave-number instability. All these scalings are similar to the scalings mentioned in Ref. 15 for the shortwave asymptotic, indicating that the large wave-number modes in the present study are qualitatively similar to the shortwave instability of interface due to the jump in normal stress difference.<sup>15</sup>

The remainder of this section deals with examining the effect of various parameters on the critical parameter  $\Gamma_c$ . The variation of  $\Gamma_c$  with  $W$  for different values of  $\beta$  and  $H$  is shown in Fig. 11. The stabilizing influence of fluid elasticity sets in for  $W \sim O(1)$ . For  $\beta \leq 0.23$ , where the finite wave-number mode is the only mode of instability,  $\Gamma_c$  increases monotonically with  $W$  following the scaling law  $\Gamma_c \sim W$ . For  $0.23 \leq \beta < 1.0$ , where the shortwave mode becomes the critical mode for highly elastic fluid, the value of  $\Gamma_c$  attains a plateau for  $W \gg 1$ . For the shortwave instability of the interface,  $\Gamma_c$  is independent of the solid thickness  $H$  as well as the Weissenberg number and depends only upon the value of  $\beta$ . On the other hand,  $\Gamma_c$  for the finite wave-number instability is found to decrease with an increase in  $H$ . As interfacial tension is known to eliminate the shortwave instability,<sup>15,16</sup> the role of interfacial tension  $T$  is also examined. Figure 12 shows the variation of  $\Gamma_c$  and  $k_c$  with the Weissenberg number for  $\beta=0.5$  and different values of  $H$  and  $T$ . The jump in  $k_c$  indicates the crossover from the finite wave number being critical to the shortwave mode being critical. For the finite wave-number mode, the interfacial tension tends to increase  $\Gamma_c$  and reduce  $k_c$ , indicating the stabilizing influence of  $T$ .

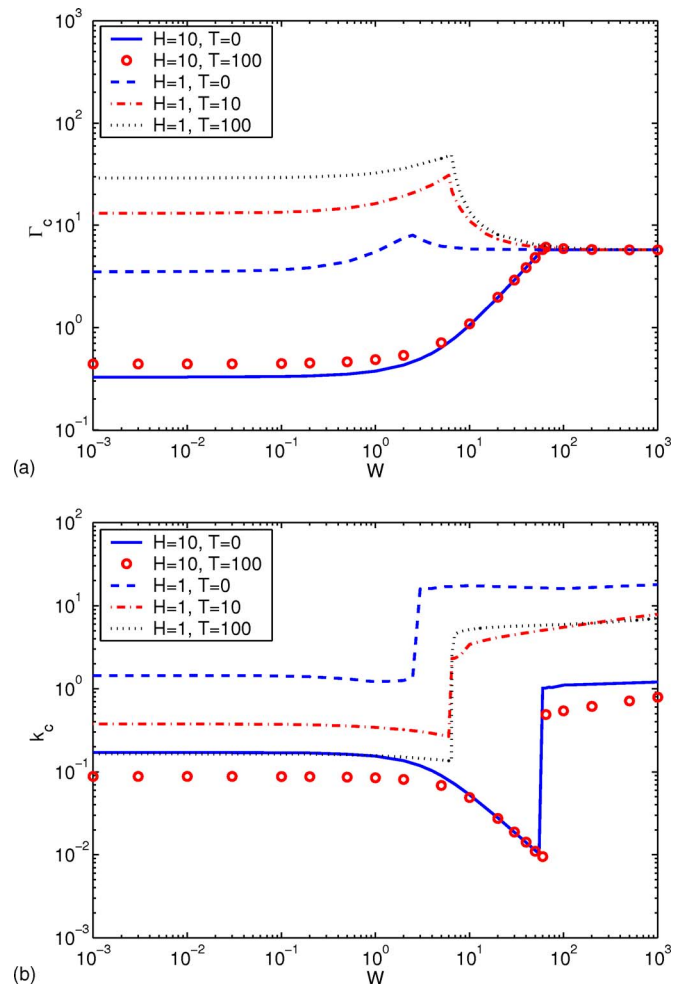


FIG. 12. Variation of  $\Gamma_c$  and the critical wave number  $k_c$  with Weissenberg number for nonzero value of interfacial tension  $T$ . The results are plotted for  $\beta=0.5$  and  $\eta_r=0$ .

However, the plateau in  $\Gamma_c$  for  $W \gg 1$  remains unchanged upon introducing the interfacial tension. Moreover, the stabilizing influence of interfacial tension on  $\Gamma_c$  diminishes as  $H$  increases. Hence,  $T$  is taken to be zero for the rest of the analysis.

The variation of  $\Gamma_c$  with  $\beta$  for different values of the Weissenberg number is shown in Fig. 13. For  $W \leq 50$ , the finite wave-number mode is the critical mode for all values of  $\beta$ . For this case,  $\Gamma_c$  increases upon reducing  $\beta$  from  $\beta = 1$ , indicating the stabilizing influence of polymer addition on the Newtonian mode of instability. For a larger Weissenberg number, the shortwave mode becomes the critical mode of instability for  $0.23 \leq \beta < 1.0$ , and  $\Gamma_c$  for such a mode is shown to be independent of  $W$ . Thus, the curve for  $W=10^4$  represents the variation of  $\Gamma_c$  with  $\beta$  for the shortwave mode and is shown to diverge as  $\beta$  approaches the value of 0.23.

Figure 14 shows  $\Gamma_c$  as a function of solid thickness  $H$  for  $W=50$  and different values of  $\beta$  and  $\eta_r$ . For the Newtonian fluid ( $\beta=1$ ), it is known that  $\Gamma_c$  and the critical wave number  $k_c$  decrease proportional to  $H^{-1}$  for  $H \gg 1$ .<sup>4</sup> They also observed that the gel viscosity has a stabilizing influence on the unstable mode such that the instability ceases to exist for a certain range of parameters for  $\eta_r \geq 1$ . For  $\eta_r=1$ , while there

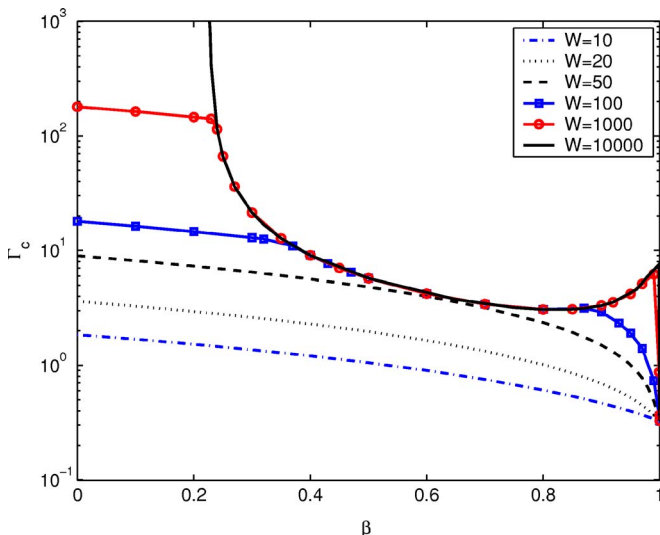


FIG. 13. Effect of  $\beta$  on critical parameter  $\Gamma_c$  for  $H=10$ ,  $\eta_r=0$ , and different values of  $W$ . The curves for different  $W$  approach a single curve in the limit  $W \gg 1$  for  $0.23 \lesssim \beta < 1$ . The limit  $\beta=1$  represents the KFP mode for the Newtonian fluid and the unstable mode for the UCM fluid is recovered at  $\beta=0$ .

are unstable traveling modes for  $H > 1$ , the interface was found to be stable for  $H < 1$ .  $\Gamma_c$  was found to diverge proportional to  $(H-1)^{-1/2}$  in the limit  $H \rightarrow 1$ . For  $\eta_r > 1$ , there are no unstable modes for  $H < \sqrt{\eta_r}$ , and  $\Gamma_c$  diverges propor-

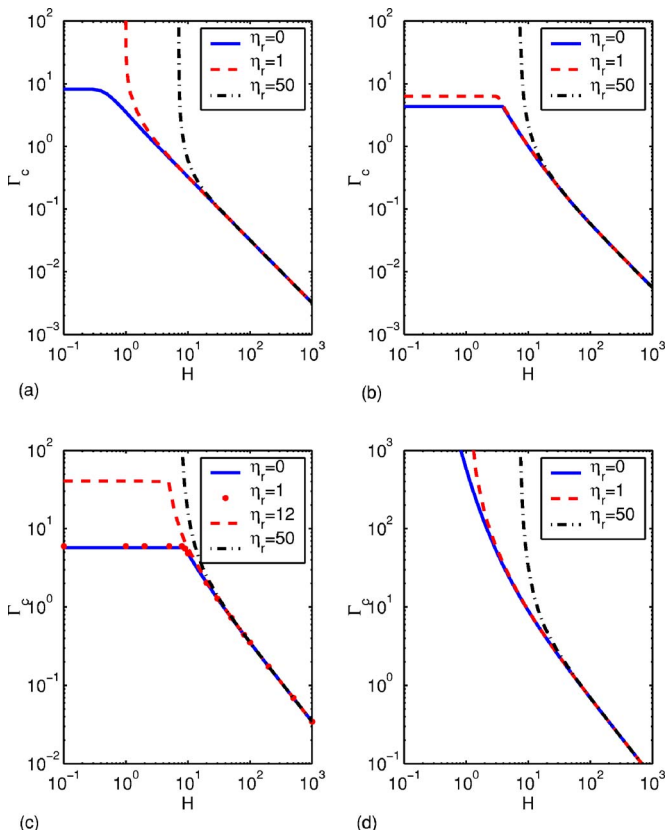


FIG. 14. Variation of  $\Gamma_c$  with the dimensionless solid thickness  $H$  for  $W=50$  and different values of solid-to-fluid viscosity ratio  $\eta_r$ . (a)  $\beta=1.0$ ; (b)  $\beta=0.95$ ; (c)  $\beta=0.5$ ; and (d)  $\beta=0$ .

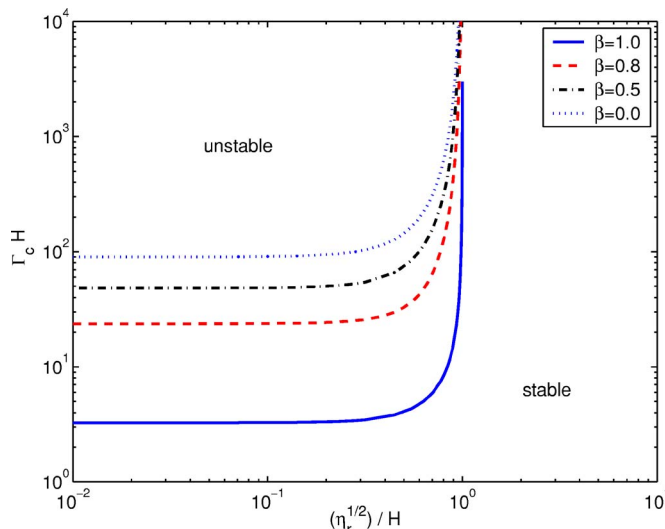


FIG. 15. Variation of  $\Gamma_c H$  with the scaled quantity  $\sqrt{\eta_r}/H$  for  $W=50$  and  $H=10$ . The plot, even though constructed for  $H=10$ , holds for any value of  $H$  where  $H \gg 1$ .

tional to  $(H-\sqrt{\eta_r})^{-1}$  as  $H$  approaches  $\sqrt{\eta_r}$ . For  $\eta_r < 1$ , the instability was found to persist for all values of  $H > 0$ . These results for the Newtonian fluid are reflected in Fig. 14(a). For the polymeric fluid, there exists a shortwave instability mode for a range of  $\beta$ . For thin solids ( $H \leq 1$ ), the shortwave mode is critical and  $\Gamma_c$  for this mode is independent of  $H$ . The variation of  $\Gamma_c$  with  $H$  for the Oldroyd-B fluid is shown in Fig. 14(b) for  $\beta=0.95$  and in Fig. 14(c) for  $\beta=0.5$ . For  $\eta_r = 0$ , the flat region for small  $H$  denotes the shortwave instability. The finite wave-number mode is critical for  $H \gg 1$  and  $\Gamma_c$  decreases proportional to  $H^{-1}$  in this limit. For  $\eta_r = 1$ , unlike for the Newtonian fluid, the shortwave instability mode exists for  $H < 1$ . An increase in gel-to-fluid viscosity ratio  $\eta_r$  has a stabilizing influence on both classes of modes. For  $\eta_r \gg 1$ , both unstable modes cease to exist for  $H < \sqrt{\eta_r}$ . Figure 14(d) shows the effect of  $H$  on  $\Gamma_c$  for  $\beta=0$ . As the finite wave-number mode is the only mode of instability for  $\beta=0$ , the unstable mode ceases to exist for  $H < \sqrt{\eta_r}$  for  $\eta_r \geq 1$ . The influence of increasing  $\eta_r$  on the least stable mode is further depicted in Fig. 15 for  $H=10$  and  $W=50$ . Here,  $\Gamma_c H$  is plotted against another scaled quantity  $\sqrt{\eta_r}/H$ . Though not shown for different values of  $H$ , this plot holds for any value of solid thickness  $H \gg 1$ . The unstable modes, either the finite wave-number mode or the shortwave mode, are present for  $\sqrt{\eta_r}/H < 1$ , and the instability ceases to exist for  $\sqrt{\eta_r}/H > 1$  as  $\Gamma_c$  diverges in the limit  $\sqrt{\eta_r}/H \rightarrow 1$  for all values of  $\beta$ . As mentioned before,  $\Gamma_c$  diverges proportional to  $(H-\sqrt{\eta_r})^{-1}$  for  $\beta=1$ . However, for the polymeric fluid,  $\Gamma_c$  diverges as  $(H-\sqrt{\eta_r})^{-2}$  for  $\beta < 1$ .

**F. Results for the flow-independent Weissenberg number  $\bar{W}$**

Since the current definition of the Weissenberg number ( $W=\lambda V/R$ ) involves the flow parameter  $V$ , we employ an alternate definition of the Weissenberg number,  $\bar{W}=\lambda G/\eta = W/\Gamma$ , which is independent of flow parameters and depends

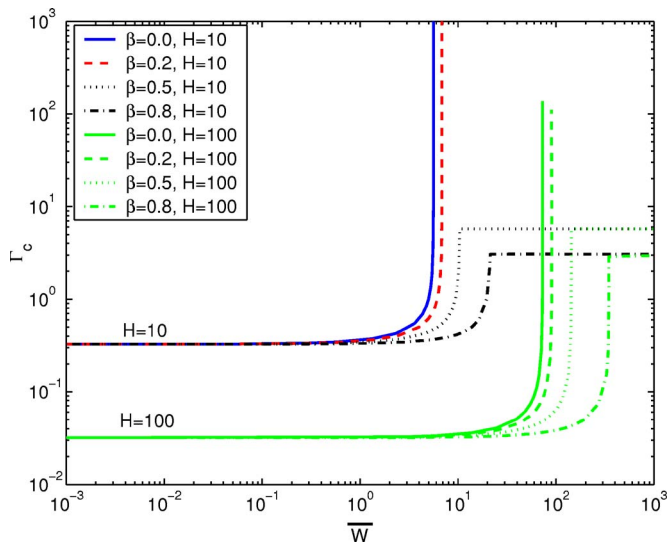


FIG. 16. Variation of  $\Gamma_c$  with the flow independent Weissenberg number  $\bar{W}$  for  $\eta_r=0$ ,  $T=0$ , and different values of  $\beta$  and  $H$ . This figure is merely a replotting of Fig. 11 using the definition  $\bar{W}=W/\Gamma$ .

only on the material properties of the fluid and the solid wall. For any comparison of the results from the present analysis with the future experimental observations, it will be very useful to have results expressed in terms of the flow-independent Weissenberg number  $\bar{W}$ . This modified definition of the Weissenberg number follows by nondimensionalizing time with  $\eta/G$ , instead of  $V/R$  used in this paper. Even though Ref. 4 adopted  $\eta/G$  as the scaling for time, we, like Ref. 11, scaled time with  $V/R$ . This scaling enabled us to continue the viscous GL modes for the solid wall ( $G \rightarrow \infty$ ) to the wall with nonzero flexibility for a finite value of Weissenberg number  $W$ . The value of critical parameter  $\Gamma = (V\eta/GR)$  for any Weissenberg number  $W$  remains the same for the new Weissenberg number  $\bar{W}=W/\Gamma$ . The behavior of the unstable mode in terms of the Weissenberg number  $\bar{W}$  is presented in this section.

Figure 16 shows the variation of  $\Gamma_c$  with  $\bar{W}$  for  $\eta_r=0$  and different values of  $\beta$  and  $H$ . This figure is the same as Fig. 11 for the flow-independent Weissenberg number  $\bar{W}$  in place of  $W$ . For  $\beta \leq 0.23$ , the fluid elasticity has a stabilizing influence on the KFP mode for the Newtonian fluid and the unstable mode ceases to exist upon increasing  $\bar{W}$  beyond a certain value  $\bar{W}_{max}$ . This  $\bar{W}_{max}$  scales as  $H$  for  $H \gg 1$ . For  $0.23 \leq \beta < 1.0$ , the influence of fluid elasticity is still stabilizing, but the instability persists for any large value of  $\bar{W}$  and there exists a plateau in  $\Gamma_c$ , independent of both  $\bar{W}$  and  $H$ , for  $\bar{W} \gg 1$ . As discussed earlier, this plateau represents the shortwave mode of instability and this mode becomes critical for  $\bar{W}/H \geq 1$ . A similar plot for nonzero  $\eta_r$  is shown in Fig. 17 for  $\beta=0.8$  and  $H=10$ . An increase in  $\eta_r$  tends to increase  $\Gamma_c$  for both the finite wave-number mode as well as the shortwave mode. Moreover, the value of  $\bar{W}$ , at which the cross-

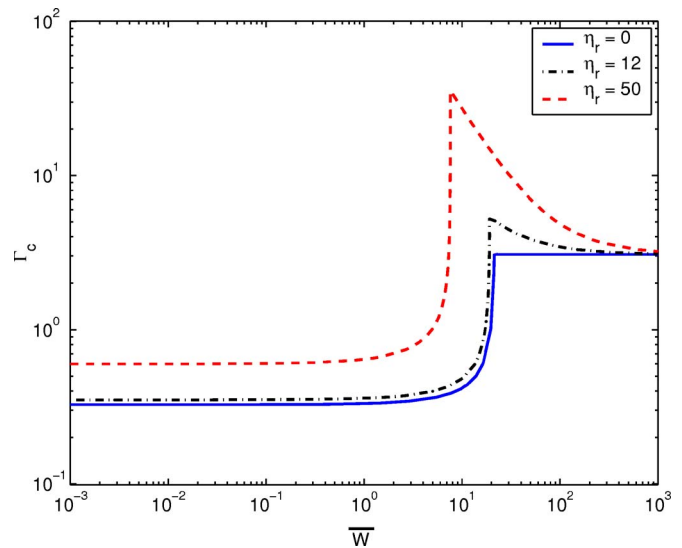


FIG. 17. Variation of  $\Gamma_c$  with the flow independent Weissenberg number  $\bar{W}$  for nonzero  $\eta_r$ . The parameters are  $\beta=0.8$ ,  $H=10$ , and  $T=0$ .

over from the finite wave-number mode being critical to the shortwave mode being critical takes place, decreases upon increasing  $\eta_r$ .

Figure 18 shows  $\Gamma_c$  as a function of  $H$  for  $\beta=0.5$  and different values of  $\bar{W}$ . The curve for  $\bar{W}=0$  represents the Newtonian fluid. The stabilizing effect of fluid elasticity on the Newtonian viscous mode is visible. The finite wave-number mode is the critical mode of instability for very thick solids with approximately  $H/\bar{W} \geq 1$ . For this mode,  $\Gamma_c$  decreases proportional to  $H^{-1}$  for  $H \gg 1$ . On the other hand, for the thin solids with  $H/\bar{W} \leq 1$ , the shortwave mode becomes the most critical mode of instability, and for this case,  $\Gamma_c$  is independent of both  $\bar{W}$  as well as  $H$ . The value of  $\Gamma_c$  for the shortwave mode is seen to be smaller than the value of  $\Gamma_c$  for

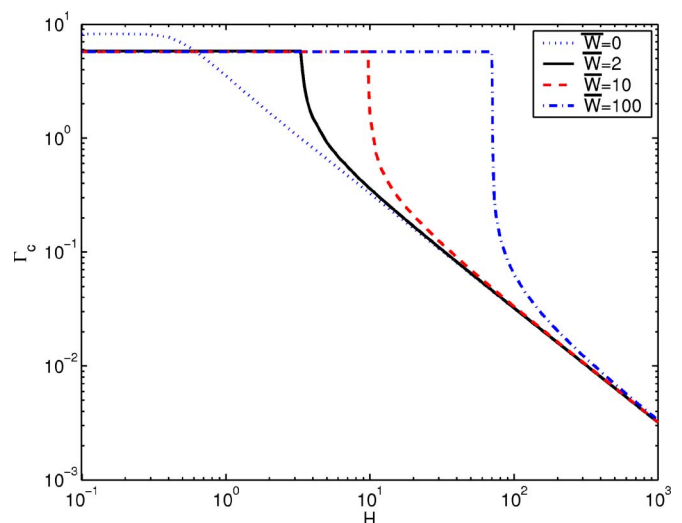


FIG. 18. Effect of solid thickness  $H$  on the critical parameter  $\Gamma_c$  for different values of flow independent Weissenberg number, keeping  $\beta=0.5$  and  $\eta_r=0$ . The curve for  $\bar{W}=0$  represents the KFP mode for the Newtonian fluid.

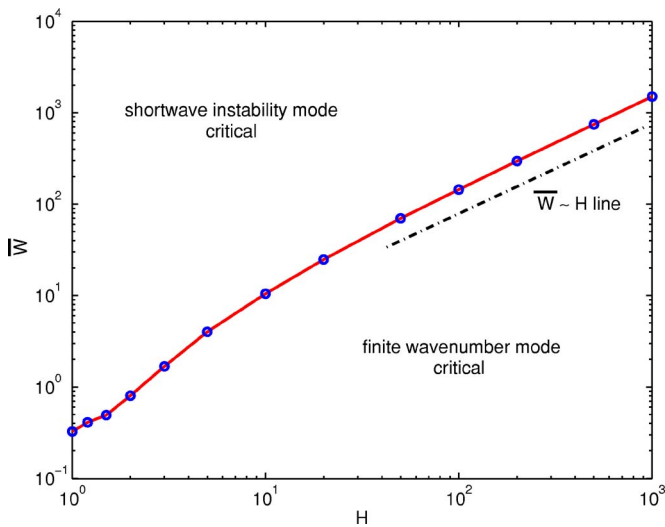


FIG. 19. Regions in the parametric space ( $\bar{W}$ - $H$ ) where each of the two classes of modes are found to be critical. The line of demarcation is obtained for a typical case  $\beta=0.5$  and  $\eta_r=0$ .

the Newtonian mode for  $H < 0.6$ , indicating the destabilizing effect of polymer addition for very thin solids.

After analyzing the effect of various parameters on  $\Gamma_c$  corresponding to the finite wave-number mode and the shortwave mode, the issue that needs to be addressed is to clearly specify the regions where one of these two unstable modes is critical. Figure 19 identifies such regions in the parametric space  $H$ - $\bar{W}$  for a typical case of  $\beta=0.5$  and  $\eta_r=0$ . For a set of parameters within the lower region, with approximately  $\bar{W}/H \lesssim 1$  for  $H \gg 1$ , the finite wave-number mode is the critical mode, whereas for the highly elastic fluid with  $\bar{W}/H \gtrsim 1$  for  $H \gg 1$ , the instability is driven by the shortwave mode. We can infer from Fig. 16 that the line of demarcation between the two regions shifts marginally upward for  $\beta$  higher than 0.5 up to  $\beta < 1$  and it shifts marginally down-

TABLE II. Scalings of  $\Gamma_c$  and  $k_c$  with  $H$  near the point of divergence for  $\eta_r \neq 0$ .

Regime	$\beta=1$	$0.23 \leq \beta < 1$	$0.12 \leq \beta < 0.23$	$\beta < 0.12$
$\eta_r < 1$	$\Gamma_c = \text{finite}$	$\Gamma_c = \text{finite}$	$\Gamma_c = \text{finite}$	$\Gamma_c \sim H^{-3}$
$H \rightarrow 0$	$k_c \sim H^{-1}$	$k_c \sim H^{-1}$	$k_c \sim H^{-1}$	$k_c = \text{finite}$
$\eta_r = 1$	$\Gamma_c \sim (H-1)^{-1/2}$	For finite $k$ mode		$\Gamma_c \sim (H-\sqrt{\eta_r})^{-2}$
$H \rightarrow 1$	$k_c \sim 1.05$	being critical,		
$\eta_r > 1$	$\Gamma_c \sim (H-\sqrt{\eta_r})^{-1}$	$\Gamma_c \sim (H-\sqrt{\eta_r})^{-2}$	$k_c \sim (H-\sqrt{\eta_r})^{3/2}$	
$H \rightarrow \sqrt{\eta_r}$	$k_c \sim (H-\sqrt{\eta_r})^{1/2}$	$k_c \sim (H-\sqrt{\eta_r})^{3/2}$		

ward for  $0.23 \leq \beta < 0.5$ . As shown earlier,  $\Gamma_c$  for the shortwave mode diverges in the limit  $\beta \rightarrow 0.23$ , and for  $\beta \leq 0.23$ , the finite wave-number mode is the only mode of instability. The important findings of our study in both regions are summarized in Table I. Here, the effect of all the parameters considered in the present analysis and the key scalings are tabulated for the finite wave-number mode as well as the shortwave mode of instability. A few of the findings listed, especially those related to the critical wave number  $k_c$ , are not illustrated by figures for the sake of brevity. The value of  $\Gamma_c$  diverges for a certain value of  $H$  for  $\eta_r \neq 0$  (see Fig. 14). The scalings near the point of divergence are summarized in Table II. These scalings for the viscoelastic fluid are compared with those obtained for the Newtonian fluid.<sup>4</sup> Unlike for the Newtonian fluid, where the scalings are different for the  $\eta_r = 1$  and  $\eta_r > 1$  regimes, the scalings are uniform for all values of  $\beta < 1$  and for  $\eta_r \geq 1$ , and they are different from the Newtonian scalings.  $\Gamma_c$  is found to diverge faster for the viscoelastic fluid than for the Newtonian fluid.

Finally, we comment on the typical parameter regime in which the recent experiments analyzing the flow past a deformable solid have been conducted.<sup>5,6,17</sup> The shear modulus  $G$  of the aqueous polymer gels used in these experiments was estimated to be around 1000–5000 N/m<sup>2</sup> and the gel

TABLE I. Summary of viscous instability modes and the dependence of  $\Gamma_c$  and  $k_c$  on various parameters.

	Finite wave-number mode	Shortwave mode
Existence	Exists for $0 \leq \beta \leq 1$ For small fluid elasticity	Exists for $0.23 \leq \beta < 1$ For highly elastic fluid
Critical	Approx. $\bar{W}/H \leq 1$ for $H \gg 1$ (see Fig. 19)	Approx. $\bar{W}/H > 1$ for $H \gg 1$ (see Fig. 19)
Effect of $W$	$\Gamma_c \sim W$ , $k_c \sim W^{-1}$ $\Gamma_c$ diverges at $\bar{W}_{\max}$	$\Gamma_c$ and $k_c$ independent of $W$
Effect of $\bar{W}$	$k_c$ drops to zero at $\bar{W}_{\max}$ $\bar{W}_{\max} \sim H$	$\Gamma_c$ and $k_c$ independent of $\bar{W}$
Effect of $H$	$\Gamma_c \sim H^{-1}$ , $k_c \sim H^{-1}$ for $H \gg 1$ (see Table II for $\eta_r \neq 0$ )	$\Gamma_c$ independent of $H$ $k_c \sim H^{-1}$ for $H > 1$
Effect of $\beta$	$\Gamma_c$ increases upon decreasing $\beta$ $k_c$ decreases upon decreasing $\beta$ $\bar{W}_{\max}$ reduces as $\eta_r$ increases	See $W=10^4$ line in Fig. 13 $k_c$ approx. independent of $\beta$ $\Gamma_c$ increases and $k_c$ decreases
Effect of $\eta_r$	$\Gamma_c$ diverges as $\sqrt{\eta_r}/H \rightarrow 1$ for $\eta_r \geq 1$ $\Gamma_c \sim (H-\sqrt{\eta_r})^{-2}$ , $k_c \sim (H-\sqrt{\eta_r})^{3/2}$	upon increasing $\eta_r$

viscosity can be estimated as  $\eta_g \approx 10^3 \text{ N s/m}^2$ . The viscosity of the Newtonian fluid used in the experiments was  $\eta \approx 1 \text{ N s/m}^2$ . However, the viscosity of a polymeric fluid is around  $\eta \approx 10\text{--}100 \text{ N s/m}^2$  and the relaxation time  $\lambda$  is anywhere between 0.001 and 0.1 s, depending on the concentration of the polymer chains. For these estimates, the flow-independent Weissenberg number  $\bar{W}$  can be in the range 0.01–50 and  $\eta_r$  around 10–100. The present analysis covers this experimentally feasible parameter regime. In this regime, both the finite wave-number mode and the shortwave mode of instability may be observed depending upon the value of solid-to-fluid thickness ratio  $H$ . However, for  $\eta_r$  close to and above 100, the instability might be observed only for  $H > 10$ , and the finite wave-number mode is likely to excite the instability.

### G. Comment for the diffusive Oldroyd-B model

The striking feature in the present analysis, different from the behavior of the UCM fluid,<sup>11</sup> is the plateau in  $\Gamma_c$  for  $0.23 \leq \beta < 1$  and  $W \gg 1$  (see Fig. 11). Along the plateau, the length scale of the disturbances is  $O(1/W)$  near the fluid-solid interface and they decay away from the interface. Hence, this highly elastic instability is similar in nature to the shortwave instability, where the relevant length scale is  $O(1/k)$ . As we have seen before, the interfacial tension up to  $T=100$  fails to eliminate this interfacial instability (see Fig. 12). In this section, we make an attempt to further examine the behavior in the limit  $W \gg 1$ . As imaginary parts of the wave speed,  $c_i$ , for the continuous spectra are given by  $-1/(kW)$  and  $-1/(k\beta W)$ , both continuous spectra approach the neutrally stable discrete mode in the limit  $W \rightarrow \infty$ . In this limit,  $c_i$  for the least stable discrete mode follows the scaling  $c_i \sim 1/W$  [see Fig. 8(b)]. This may suggest that the least stable discrete mode is affected by the presence of continuous spectra nearby. The continuous spectra are the result of singularity in the fluid governing Eq. (29) which, in turn, is due to the hyperbolic nature of the evolution equation for the conformation tensor [Eq. (8)]. The addition of an artificial diffusive term is known to eliminate the singularity and hence destroy the continuous spectra.<sup>18</sup> The Oldroyd-B model with artificial diffusivity looks like

$$D_t \mathbf{c} = -\frac{(\mathbf{c} - \mathbf{I})}{W} + \frac{1}{\text{Pe}} \nabla^2 \mathbf{c}, \quad (41)$$

where the Peclet number is defined as the ratio of polymer diffusion time scale to the flow time scale,  $\text{Pe} = RV/D_{tr}$ , with  $D_{tr}$  being the translational diffusivity of the polymer chains. The classical Oldroyd-B model is recovered in the limit  $\text{Pe} \rightarrow \infty$ . For the boundary conditions for the conformation tensor, necessitated by the additional diffusive term, Suresh Kumar and Beris<sup>18</sup> suggested the use of the classical Oldroyd-B model at the wall. That means the evolution equation (41) for  $\mathbf{c}$  with  $\text{Pe} \rightarrow \infty$  is forced to satisfy at the top wall and at the fluid-gel interface. Analyzing the stability of the diffusive Oldroyd-B fluid, we construct the neutral stability diagram in the  $\Gamma_t$ - $W$  plane for different values of the Peclet number, as shown in Fig. 20. The stability curve for the diffusive Oldroyd-B model is on top of the curve for the classical

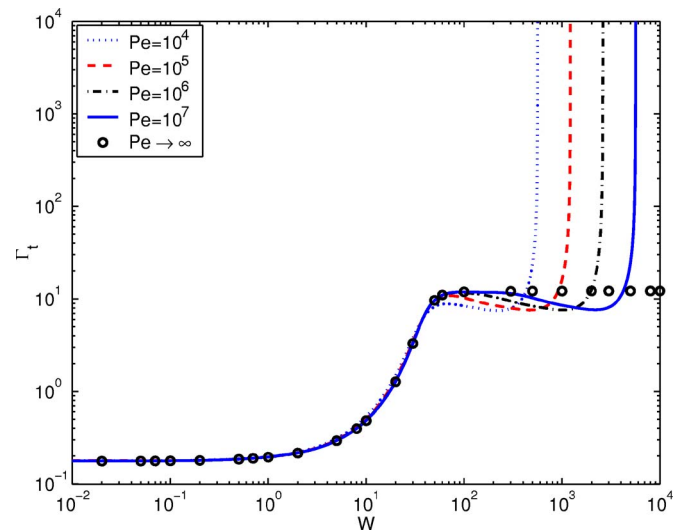


FIG. 20. Variation of  $\Gamma_t$  with Weissenberg number  $W$  for the Oldroyd-B model with an artificial diffusivity. The scaled diffusivity is given by the inverse of the Peclet number. The parameters are  $k=0.05$ ,  $\beta=0.5$ ,  $H=20$ , and  $\eta_r=0$ . In the limit  $\text{Pe} \rightarrow \infty$ , the classical Oldroyd-B fluid is recovered.

Oldroyd-B model up to  $W \approx 100$ , whereas for the large Weissenberg number, the behavior is drastically different for both models. The flat region present for the classical Oldroyd-B fluid is nonexistent and the unstable mode ceases to exist for  $W \gg 1$ . The variation of  $\Gamma_t$  with wave number  $k$  is shown in Fig. 21 for  $\text{Pe}=10^5$ . Here, the shortwave instability present for the classical Oldroyd-B model disappears by the addition of a diffusive term. Also, there exist two local minima along the  $\Gamma$ - $k$  curve and the global minimum, which corresponds to the critical point  $(k_c, \Gamma_c)$ , shifts from the first minimum to the second one for  $W \geq 100$ . Figure 22 shows the variation of  $\Gamma_c$  with the flow-independent Weissenberg number  $\bar{W}$  for  $\text{Pe} = 10^6$ . As a significant departure from the classical Oldroyd-B behavior, the plateau in  $\Gamma_c$  does not exist, and the system is found to be stable for highly elastic fluid. The

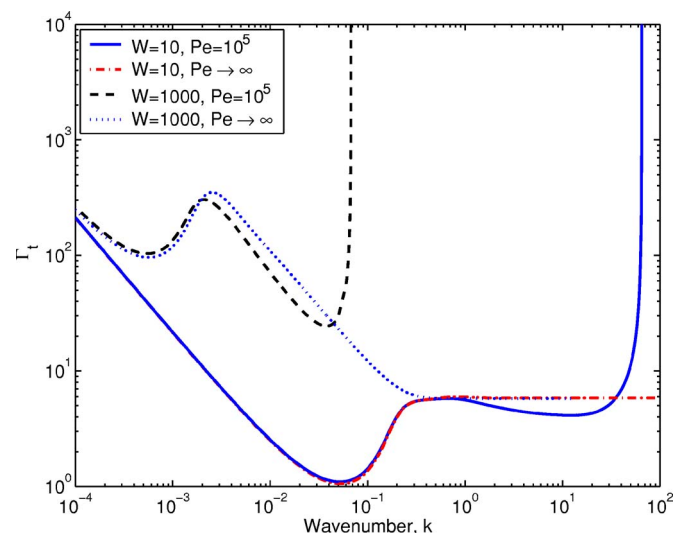


FIG. 21. Neutral stability curve  $\Gamma_t$  versus  $k$  for the diffusive Oldroyd-B model for  $H=10$ ,  $\beta=0.5$ , and  $\eta_r=0$ . The corresponding curves for the classical Oldroyd-B model are also shown in the limit  $\text{Pe} \rightarrow \infty$ .

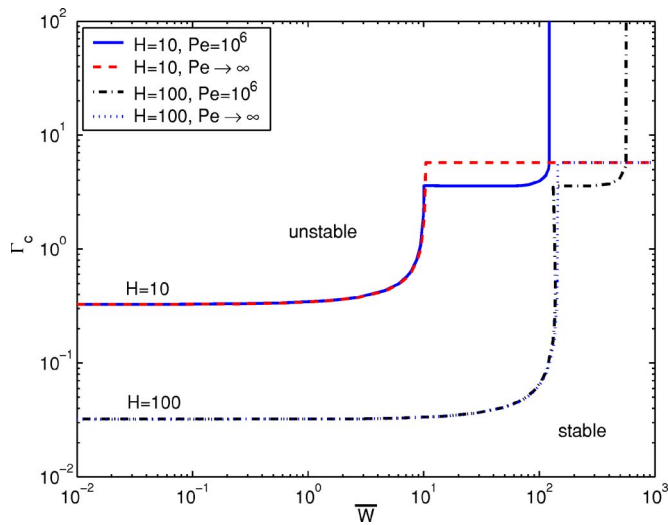


FIG. 22. Variation of  $\Gamma_c$  with the flow-independent Weissenberg number  $\bar{W}$  for the diffusive Oldroyd-B model for  $Pe=10^6$ ,  $\beta=0.5$ , and  $\eta_r=0$  and different values of  $H$ . The plateau in  $\Gamma_c$  for the classical Oldroyd-B model is eliminated, rendering stability for  $\bar{W} \gg 1$ .

results for the diffusive Oldroyd-B model are presented only to highlight the discrepancy between the two models in the limit of large Weissenberg number. In this limit, the shortwave instability for the classical Oldroyd-B fluid seems to be the feature specific to the model. Such instability modes are shown to disappear for the diffusive Oldroyd-B model. However, the addition of diffusivity in a homogeneous polymeric solution is physically unreasonable and only serves to stabilize the numerical scheme. Since the polymer diffusion is a consequence of local nonhomogeneity, it is essential to incorporate the polymer number density and its spatial variations in the model. A model capturing the rheology and mass transfer phenomenon in a dilute polymer solution with spatially varying distribution has been derived by a number of researchers.<sup>19-21</sup> The stability behavior of such nonhomogeneous polymeric fluids in the limit of high elasticity may be investigated in future studies.

#### IV. CONCLUSIONS

A linear stability analysis of plane Couette flow of a viscoelastic fluid modeled as an Oldroyd-B fluid past a linear viscoelastic solid surface has been carried out in the flow regime  $Re \ll 1$  to analyze the *viscous modes* of instability. Beginning with the growth rate eigenspectrum for the rigid wall problem,<sup>10</sup> the wall is made compliant by assigning a nonzero value to the wall flexibility parameter  $\Gamma = V\eta/(GR)$ , and the evolution of the eigenspectrum with an increasingly flexible surface is studied. It was found that a few new modes emerge from the continuous spectra upon increasing the wall flexibility. But these modes remain stable for any large value of  $\Gamma$ . However, one of the discrete modes existing for the hard wall becomes unstable when the wall elasticity parameter  $\Gamma$  exceeds a certain critical value  $\Gamma_c$ , indicating the destabilizing effect of wall flexibility. Similar destabilization in the flexible wall limit is reported for the upper convected Maxwell (UCM) fluid,<sup>11</sup> which is the spe-

cial case of the Oldroyd-B model for zero solvent viscosity ( $\beta=0$ ). The unstable polymeric viscous mode is, in fact, the continuation of the viscous instability for the Newtonian fluid flow past a flexible surface (referred to as the KFP mode)<sup>4</sup> to the fluid with finite elasticity. The influence on the critical parameter  $\Gamma_c$ , of the numerous parameters, like the Weissenberg number, the solvent viscosity parameter  $\beta$ , the thickness ratio of solid-to-fluid layers  $H$ , and the ratio of gel-to-fluid viscosity  $\eta_r$ , is studied. An important feature of the present problem is the existence of the additional shortwave instability modes, apart from the finite wave-number modes. While the later modes of instability were present in the previous analyses, the shortwave nature of instability was absent for the limiting cases of the Newtonian fluid ( $\beta=1$ ) and the UCM fluid ( $\beta=0$ ). These shortwave instability modes, which are believed to be due to a jump in the first normal stress difference for the base state across the interface, become the fastest growing modes for a highly elastic fluid. It was shown that the surface force with dimensionless interfacial tension  $T$  as large as 100 fails to eliminate the shortwave instability for fluids with Weissenberg number  $W \gg 1$ .

The fluid elasticity has a stabilizing effect on the unstable KFP mode for the Newtonian fluid. For  $\beta \leq 0.23$ , the shortwave instability is absent and the flow becomes stable for any value of flow independent Weissenberg number  $\bar{W} > \bar{W}_{max}$ . This finding is qualitatively similar to the behavior of the UCM fluid.<sup>11</sup> The maximum Weissenberg number for the instability to exist,  $\bar{W}_{max}$ , increases proportional to  $H$  for  $H \gg 1$ . For  $0.23 \leq \beta < 1$ , both the shortwave and the finite wave number modes coexist. For low to moderate Weissenberg number (approximately  $\bar{W}/H < 1$ ), the finite wave-number mode is found to be the most critical for transition. For this case,  $\Gamma_c$  decreases proportional to  $H^{-1}$  for  $H \gg 1$  and it increases monotonically upon reducing  $\beta$  from  $\beta=1$ , indicating the stabilizing influence of polymer addition. On the other hand, for highly elastic fluids (approximately  $\bar{W}/H > 1$ ), the most unstable modes are of a shortwave nature. In this case, the instability persists for any large value of  $\bar{W}$ , and  $\Gamma_c$  is independent of  $\bar{W}$  as well as the dimensionless solid thickness  $H$ . Upon reducing  $\beta$ , the value of  $\Gamma_c$  for the shortwave mode decreases initially for very dilute solutions ( $\beta$  close to 1) and then increases such that  $\Gamma_c$  diverges in the limit  $\beta \rightarrow 0.23$ . Thus, the shortwave instability ceases to exist for  $\beta \leq 0.23$ . The regions showing each kind of mode being critical are shown in the parametric space ( $\bar{W}$ - $H$ ). The solid-to-fluid viscosity ratio  $\eta_r$  has a stabilizing effect on both classes of modes such that for large  $\eta_r$ , the instability ceases to exist for a finite Weissenberg number fluid. It is shown that  $\Gamma_c$  diverges in the limit  $\sqrt{\eta_r}/H \rightarrow 1$  for  $H \gg 1$  and the flow becomes stable for  $\sqrt{\eta_r}/H > 1$ . The important findings of the present analysis are summarized in Table I.

An important outcome of the present study, the instability in the limit  $\bar{W} \gg 1$ , appears to be specific to the Oldroyd-B model used to represent the viscoelastic fluid. This instability can be attributed to the existence of the continuous spectra, which are the characteristics of the

Oldroyd-B model. This was suggested by a brief study using the diffusive Oldroyd-B model, which is known to eliminate the continuous spectra. It is shown that by introducing a small artificial diffusion term in the evolution equation of the polymer chain conformation tensor, the shortwave instability disappears and only the finite wave-number modes of instability are present. Consequently, the instability in the limit  $\bar{W} \gg 1$  ceases to exist and the system was found to be stable for any Weissenberg number  $\bar{W} > \bar{W}_{\max}$ .

- <sup>1</sup>P. Krindel and A. Silberberg, "Flow through gel-walled tubes," *J. Colloid Interface Sci.* **71**, 39 (1979).
- <sup>2</sup>V. Kumaran, "Classification of instabilities in the flow past flexible surfaces," *Curr. Sci.* **79**, 776 (2000).
- <sup>3</sup>V. Shankar, "Linear and weakly nonlinear stability of fluid flow through flexible tubes and channels," Ph.D. thesis, Indian Institute of Science (2000).
- <sup>4</sup>V. Kumaran, G. H. Fredrickson, and P. Pincus, "Flow induced instability of the interface between a fluid and a gel at low Reynolds number," *J. Phys. II* **4**, 893 (1994).
- <sup>5</sup>V. Kumaran and R. Muralikrishnan, "Spontaneous growth of fluctuations in the viscous flow of a fluid past a soft interface," *Phys. Rev. Lett.* **84**, 3310 (2000).
- <sup>6</sup>R. Muralikrishnan and V. Kumaran, "Experimental study of the instability of the viscous flow past a flexible surface," *Phys. Fluids* **14**, 775 (2002).
- <sup>7</sup>V. Kumaran, "Stability of the viscous flow of a fluid through a flexible tube," *J. Fluid Mech.* **294**, 259 (1995).
- <sup>8</sup>V. A. Gorodtsov and A. I. Leonov, "On a linear instability of a plane parallel Couette flow of viscoelastic fluid," *J. Appl. Math. Mech.* **31**, 310 (1967).
- <sup>9</sup>M. Renardy, "Rigorous stability proof for plane Couette flow of an upper convected Maxwell fluid at zero Reynolds number," *Eur. J. Mech. B/Fluids* **11**, 511 (1992).
- <sup>10</sup>H. J. Wilson, M. Renardy, and Y. Renardy, "Structure of the spectrum in zero Reynolds number shear flow of the UCM and Oldroyd-B liquids," *J. Non-Newtonian Fluid Mech.* **80**, 251 (1999).
- <sup>11</sup>V. Shankar and S. Kumar, "Instability of viscoelastic plane Couette flow past a deformable wall," *J. Non-Newtonian Fluid Mech.* **116**, 371 (2004).
- <sup>12</sup>S. Kumar and V. Shankar, "Instability of high-frequency modes in viscoelastic plane Couette flow past a deformable wall at low and finite Reynolds number," *J. Non-Newtonian Fluid Mech.* **125**, 121 (2005).
- <sup>13</sup>L. Srivatsan and V. Kumaran, "Flow induced instability of the interface between a fluid and a gel," *J. Phys. II* **7**, 947 (1997).
- <sup>14</sup>V. Kumaran, "Stability of fluid flow through a flexible tube at intermediate Reynolds number," *J. Fluid Mech.* **357**, 123 (1998).
- <sup>15</sup>Y. Renardy, "Stability of the interface in two-layer Couette flow of the upper convected Maxwell liquids," *J. Non-Newtonian Fluid Mech.* **28**, 99 (1988).
- <sup>16</sup>V. Gkanis and S. Kumar, "Instability of creeping Couette flow past a neo-Hookean solid," *Phys. Fluids* **15**, 2864 (2003).
- <sup>17</sup>M. D. Eggert and S. Kumar, "Observations of instability, hysteresis, and oscillation in low-Reynolds number flow past polymer gels," *J. Colloid Interface Sci.* **278**, 234 (2004).
- <sup>18</sup>R. Sureshkumar and A. N. Beris, "Effect of artificial stress diffusivity on the stability of numerical calculations and the flow dynamics of time-dependent viscoelastic flows," *J. Non-Newtonian Fluid Mech.* **60**, 53 (1995).
- <sup>19</sup>A. V. Bhave, R. C. Armstrong, and R. A. Brown, "Kinetic theory and rheology of dilute, non-homogeneous polymer solutions," *Chem. Phys.* **14**, 2988 (1991).
- <sup>20</sup>V. G. Mavrantzas and A. N. Beris, "Modeling of the rheology and flow-induced concentration changes in polymer solutions," *Phys. Rev. Lett.* **69**, 273 (1992).
- <sup>21</sup>H. C. Öttinger, "Incorporation of polymer diffusivity and migration into constitutive equations," *Rheol. Acta* **31**, 14 (1992).